

γ -ray spectroscopy of neutron-deficient ^{110}Te . I. Low- and intermediate-spin structures

E. S. Paul,¹ A. J. Boston,¹ C. J. Chiara,^{2,*} M. Devlin,^{3,†} D. B. Fossan,² S. J. Freeman,⁴ D. R. LaFosse,³ G. J. Lane,^{2,‡} M. J. Leddy,⁴ I. Y. Lee,⁵ A. O. Macchiavelli,⁵ P. J. Nolan,¹ D. G. Sarantites,³ J. M. Sears,² A. T. Semple,¹ J. F. Smith,^{2,4,§} and K. Starosta^{2,||}

¹*Oliver Lodge Laboratory, University of Liverpool, Liverpool L69 7ZE, United Kingdom*

²*Department of Physics and Astronomy, State University of New York at Stony Brook, Stony Brook, New York 11794-3800, USA*

³*Department of Chemistry, Washington University, St. Louis, Missouri 63130, USA*

⁴*Schuster Laboratory, University of Manchester, Brunswick Street, Manchester M13 9PL, United Kingdom*

⁵*Nuclear Science Division, Lawrence Berkeley National Laboratory, Berkeley, California 94720, USA*

(Received 12 October 2006; published 25 September 2007)

Excited states have been populated in ^{110}Te via the $^{58}\text{Ni}(^{58}\text{Ni},\alpha 2p\gamma)$ reaction at 250 MeV. The Gammasphere γ -ray spectrometer was augmented with ancillary detectors for charged-particle and neutron detection in order to provide clean channel selection. The known level scheme of ^{110}Te has been greatly expanded with the addition of many new structures. Above spin 8^+ , negative-parity structures become yrast. The level scheme of ^{110}Te below $30\hbar$ is discussed in this paper, including possible evidence for octupole correlations inferred from strong $B(E1)$ strengths.

DOI: [10.1103/PhysRevC.76.034322](https://doi.org/10.1103/PhysRevC.76.034322)

PACS number(s): 27.60.+j, 21.10.Re, 23.20.Lv, 25.70.Hi

I. INTRODUCTION

A wide variety of nuclear-structure phenomena is associated with neutron-deficient nuclei in close proximity to the $Z = 50$ closed shell. These nuclei provide an ideal case in which to observe competition between collective and single-particle degrees of freedom. At low spin, nuclei in this region have near-spherical configurations. This manifests itself in the observation of irregular single-particle level structures, typified in nuclei such as ^{108}Sn [1] and ^{109}Sb [2]. Even-even tellurium isotopes show behavior typical of vibrational structures in a weakly deformed nucleus at low spin, and multiphonon excitations describe the observed ground-state band structures; the latest systematics down to ^{106}Te can be found in Ref. [3]. At higher spin, two-quasiparticle configurations coupled to the underlying weakly deformed structure become yrast. High-spin collectivity (enhanced quadrupole deformation) in this mass region can, however, be induced by particle-hole (p-h) excitations, which involve the excitation of one or more $g_{9/2}$ protons across the $Z = 50$ shell gap [4,5]. Lifetime measurements of levels in high-spin terminating bands of ^{108}Sn and ^{109}Sb [6] and ^{112}Te [7] have confirmed such collectivity.

Prior to this work, no evidence for collective rotational band structures was cited in ^{110}Te [8,9]. Indeed, the low-spin level

scheme presented a vibrational-like structure. Furthermore, a number of enhanced $E1$ transitions suggested octupole collectivity at higher spin [8]. The present paper includes an expanded low- and intermediate-spin decay scheme ($I < 30$), which confirms and extends the observation of enhanced $E1$ transitions. In an accompanying paper [10], several new high-spin terminating structures, extending well beyond $I = 30$, are presented.

II. EXPERIMENTAL DETAILS

Excited states in neutron-deficient $A \sim 110$ nuclei were populated with the $^{58}\text{Ni}(^{58}\text{Ni},\alpha\alpha\gamma p\gamma)$ fusion-evaporation reaction. The experiment was performed at the Lawrence Berkeley National Laboratory, using a 250 MeV ^{58}Ni beam supplied by the 88 in. cyclotron. The beam was incident on a thin self-supporting ^{58}Ni target of nominal thickness $500\ \mu\text{g}/\text{cm}^2$, isotopically enriched to $>97\%$. The Gammasphere γ -ray spectrometer [11], containing 83 high-purity germanium (HPGe) detectors, was used in conjunction with the Microball charged-particle detector, containing 95 CsI(Tl) scintillators [12], and an array of 15 neutron detectors in order to provide clean exit-channel selection (x, y, z). Coincident escape-suppressed events, occurring within a prompt time window of 50 ns, were recorded to tape when at least three γ rays were detected in coincidence with a charged-particle detected in the Microball; the number of associated neutrons was also recorded. Under this condition, 1.4×10^9 events were collected in four days of beam time.

Energy and efficiency calibrations for the Gammasphere array were achieved using standard ^{152}Eu , ^{60}Co , and ^{182}Ta sealed radioactive sources, which were mounted at the target position. The data acquired from these sources enabled a good knowledge of the response of the spectrometer to be found for the broad range of γ -ray energies corresponding to those observed in this work.

*Present address: Department of Chemistry, Washington University, St. Louis, Missouri 63130, USA.

†Present address: Los Alamos National Laboratory, Los Alamos, New Mexico 87545, USA.

‡Present address: Department of Nuclear Physics, Research School of Physical Sciences and Engineering, Australian National University, Canberra ACT 0200, Australia.

§Present address: School of Engineering and Science, University of Paisley, Paisley, PA1 2BE, United Kingdom.

||Present address: National Superconducting Cyclotron Laboratory, Michigan State University, East Lansing, Michigan 48824, USA.

III. DATA ANALYSIS

A. Kinematic Doppler correction

To access neutron-deficient nuclei in the mass $A \sim 110$ region, such as ^{110}Te , the use of a symmetric reaction is required. Such an approach, combined with the use of a thin target, results in the residual nuclei having a large recoil velocity ($v \sim 0.047c$). The observed γ rays therefore exhibit both a Doppler shift and a Doppler broadening in their measured energies. The Doppler correction has been achieved by knowing the recoil velocity v of residual nuclei and the angle θ of each HPGe detector. The use of segmented detector technology in the Gammasphere array allows the effective opening angle of the HPGe detectors to be reduced, further improving the observed γ -ray resolution.

The assumption that the recoils are emitted along the beam direction, while valid for fusion-evaporation reactions which result in heavy ($A \geq 130$) recoiling nuclei, becomes less valid for lighter systems. The emission of light particles (particularly α particles) has the effect of broadening the recoil cone, which results in γ rays with a poor resolution being observed. The quality of the spectra studied in this work has greatly benefited from a kinematic Doppler reconstruction [13] performed using the Microball. This approach typically yielded an improvement of 30% in the resolution of γ -ray transitions for the ^{110}Te exit channel. For example, the full-width half maximum (FWHM) of a 1 MeV γ ray was reduced from ~ 8 keV to ~ 5 keV.

B. Channel selection

The $^{58}\text{Ni}+^{58}\text{Ni}$ reaction produces ^{110}Te by the $\alpha 2p$ channel ($x = 1, y = 2, z = 0$). Other strong evaporation channels at the beam energy of 250 MeV include $3p$ (^{113}I), $4p$ (^{112}Te), and $\alpha 3p$ (^{109}Sb). The Microball was used to select $\alpha 2p$ events with additionally no neutrons detected. The detection efficiencies for protons ($\sim 85\%$) and α particles ($\sim 65\%$) means that some contamination arises from channels where an evaporated proton or α particle is “missed.” Note, however, that the low neutron efficiency ($\sim 5\%$) is of-set by the severely hindered neutron-emission probability in this neutron-deficient region such that contamination from $\alpha 2pxn$ channels ($^{108,109}\text{Te}$) is negligible.

To further improve the channel selection, the bismuth-germanate (BGO) anti-Compton shield elements of the Gammasphere HPGe detectors were used as a γ -ray fold and sum-energy selection device. By removing the Hevimet collimators from the front of the HPGe detectors, the front of the BGO suppression shields were exposed, allowing γ rays to directly strike the shield elements. The energy-spin (E^*-I) entry point for reaction products produced in a fusion-evaporation reaction depends upon which reaction channel formed the product. For example, residual nuclei formed by the evaporation of fewer particles leave the nucleus in a state of higher spin and excitation energy than channels with higher particle emission multiplicities. The number of detectors that fire (fold), k , gives an estimate of the total γ -ray multiplicity of the cascade (related to the initial angular momentum I of the system). The total sum energy H emitted in a decay cascade gives information on the initial excitation

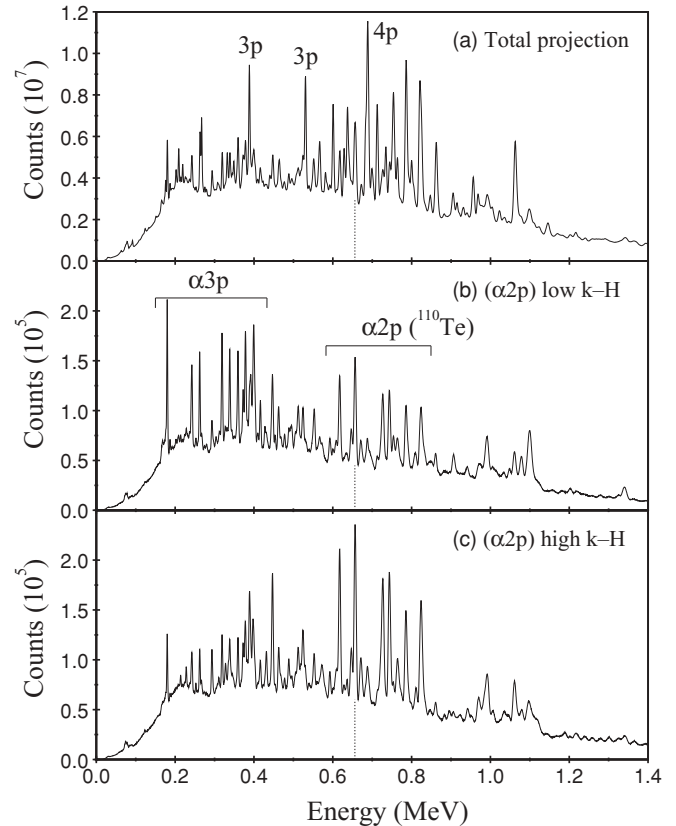


FIG. 1. Gamma-ray spectra produced following the $^{58}\text{Ni}+^{58}\text{Ni}$ reaction. A projection of the total data is shown in (a), while the effects of $\alpha 2p$ charged-particle selection in addition to low $k-H$ (b) and high $k-H$ (c) conditions are also shown. The position of the 657 keV ($2^+ \rightarrow 0^+$) transition of ^{110}Te is indicated by the dashed line in each spectrum. The strong transitions evident between 0.2 and 0.4 MeV in (b), arising from contamination from the $\alpha 3p$ (^{109}Sb) channel, are clearly suppressed in (c).

energy E^* of the nucleus. By setting off-line software gates on a two-dimensional $k-H$ plot, a significant improvement in the quality of the channel selection was achieved. The effect of $k-H$ gating is illustrated in Fig. 1, where it can be seen that a high $k-H$ selection enhances the ^{110}Te transitions [Fig. 1(c)]. The high $k-H$ condition reduces contamination from the $\alpha 3p$ (four-particle) channel leading to ^{109}Sb [see Fig. 1(b)]. γ -ray spectra gated by combinations of protons, neutrons, and α particles, in addition to appropriate $k-H$ cuts, are shown in Fig. 2, where several tellurium isotopes ($A = 109-112$) have been selected.

The initial 1.4×10^9 events were reduced to 6.2×10^7 following the selection of the ^{110}Te exit channel. The data were then unfolded into constituent quadruple (γ^4) coincidence events and replayed into a RADWARE-format [14] four-dimensional hypercube with a nonlinear gain compression of two channels per FWHM. Transitions between 33 keV and 2.8 MeV were stored in the hypercube. A total of 2.4×10^8 γ^4 events were incremented. The 4DG8R [15] graphical analysis package facilitated a detailed investigation of the data, allowing single-, double-, and triple-gated coincidence γ -ray spectra to be examined.

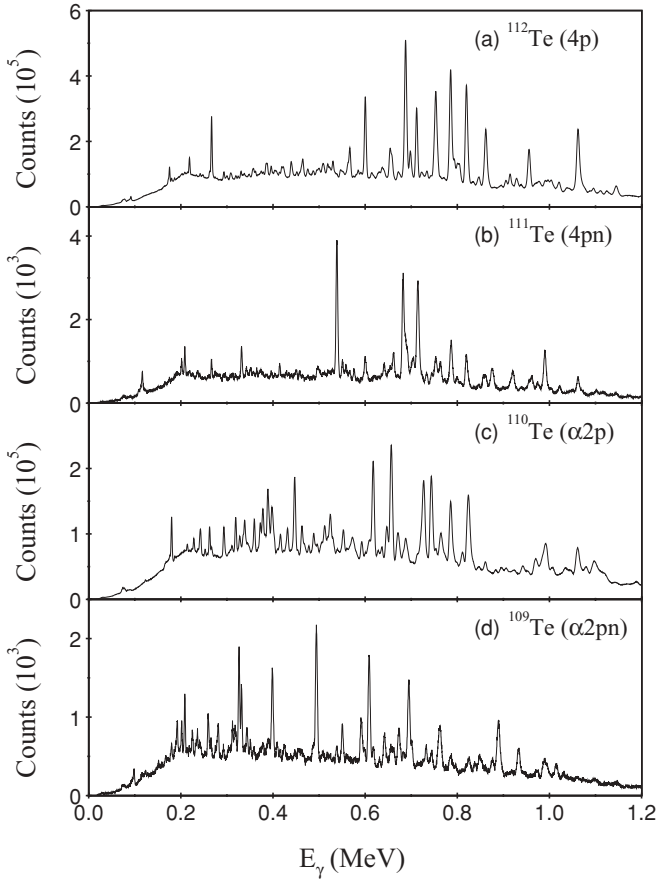


FIG. 2. Particle-gated γ -ray spectra produced following the $^{58}\text{Ni}+^{58}\text{Ni}$ reaction, selecting tellurium isotopes.

C. Level scheme construction

The ordering of transitions within the proposed level scheme is based on coincidence and relative intensity arguments. The relative intensities were obtained from a global fit of the γ - γ coincidence intensities in a two-dimensional projection (matrix) of the hypercube [14]. Such an approach may lead to systematic errors of up to 10% on the transition intensities when including angular-correlation effects and statistics of the unfolding procedure.

To assist in assigning spins and parities to transitions in the level scheme, γ -ray multipolarities were extracted from the data by conducting an angular-correlation analysis using the method of direction correlation from oriented states (DCO) [16]. Two asymmetric matrices were constructed, containing unfolded γ - γ coincidences from the HPGe detectors close to $\theta = 90^\circ$ (with respect to the beam direction) against all angles, and HPGe detectors close to $\theta = 130^\circ$ (and 50°) against all angles. By placing gates on the “all” axes of each matrix, one-dimensional spectra could be projected out and an experimental angular-intensity ratio,

$$R = \frac{I_{\gamma\gamma}[\theta \approx 130^\circ(50^\circ)]}{I_{\gamma\gamma}[\theta \approx 90^\circ]}, \quad (1)$$

evaluated for the majority of the γ -ray transitions. This approach yields values of $R \approx 1.0$ and 0.63 for pure stretched quadrupole and dipole transitions, respectively.

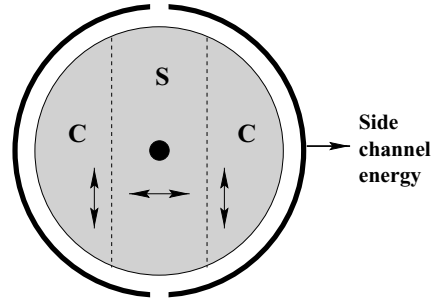


FIG. 3. Schematic diagram of a Gammasphere segmented detector where the outer contact of the Ge crystal is split into two. A vertically Compton-scattered event is more likely to be confined (C) to one side of the detector. A horizontally Compton-scattered event is more likely to be shared (S) by both sides of the detector.

A measurement of the linear polarization for some of the more intense transitions has also been attempted, enabling the electromagnetic character of the γ -ray transitions to be determined. This made use of the segmented Gammasphere detectors, which provide a facility for observing the fraction of Compton-scattered events which share their energy between both sides of the detector (“shared” S) and those which confine themselves to one side (“confined” C), as shown in Fig. 3.

The experimental linear polarization for the Gammasphere array may be defined as [17]

$$P = \frac{1}{Q} \frac{1}{\sqrt{\eta}} \left[\frac{\eta C - S}{C + S} \right], \quad (2)$$

where C and S represent the number of confined and shared events, respectively. Q is the γ -ray linear-polarization sensitivity, a function of γ -ray energy, and is taken from Ref. [17]. The parameter η , the relative efficiency for the detection of confined and shared events, was obtained using a ^{152}Eu radioactive source placed at the target position; the results are shown in Fig. 4.

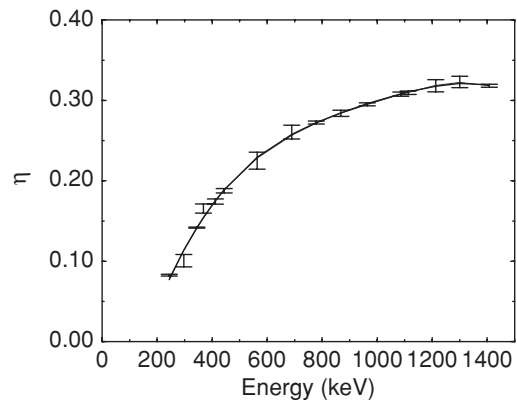


FIG. 4. Measurement of the relative efficiency η for the detection of confined and shared events in the Gammasphere segmented detectors.

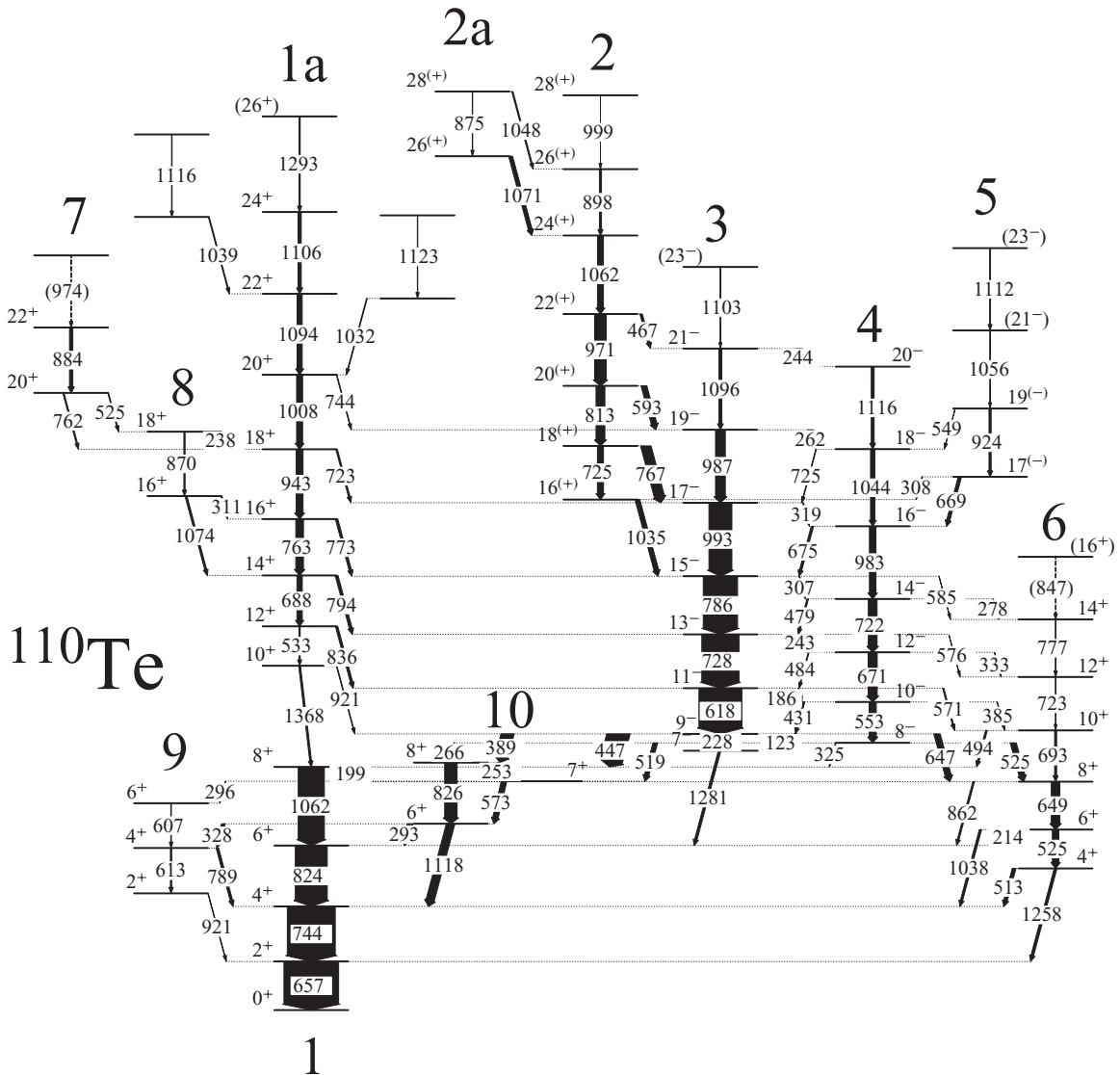


FIG. 5. Level scheme deduced for ^{110}Te for $I < 30$. The transition energies are given in keV and the width of the arrows are proportional to their intensities.

IV. EXPERIMENTAL RESULTS

The low- and intermediate-spin ($I < 30$) level scheme deduced for ^{110}Te from this work is presented in Fig. 5 showing band structures labeled 1–10. Examples of background-subtracted γ -ray coincidence spectra are shown in Fig. 6. Properties of the transitions are listed in Table I. These results are discussed in more detail in the following sections. The high-spin level scheme of ^{110}Te , up to $I \sim 45$, is presented in the accompanying paper [10].

A. Low-spin positive-parity structures

The low-spin ^{110}Te level scheme is in general a complicated collection of many irregularly spaced levels, containing a number of doublet or near doublet transitions. The ordering of transitions is based primarily on coincidence relationships and intensity arguments.

1. Bands 1 and 1a

Band 1 is based on the ^{110}Te ground state. It includes four members and is yrast up to spin 8^+ . A coincidence γ -ray spectrum is shown in Fig. 6(a). The transitions in band 1 are clearly visible along with a large number of other γ rays associated with this nucleus. Band 1a, consisting of eight stretched $E2$ transitions, is a newly identified structure and has been observed up to a proposed spin $I^\pi = 26^+$. A very weak transition of 1368 keV and assumed $E2$ nature is observed to directly link band 1a to band 1 ($10^+ \rightarrow 8^+$). The band has been assigned with positive parity following inferred confirmation through angular-intensity analysis showing the dipole ($E1$) nature of the six linking transitions observed to decay to negative-parity band 3. The intensity profile of band 1a is such that below 12^+ the structure contains almost no intensity, suggesting the configuration is strongly disfavored at this spin. Indeed it is only with the greater selectivity afforded by a

TABLE I. Measured properties of the low-spin ($I < 30$) γ -ray transitions assigned to ^{110}Te which are shown in Fig. 5.

E_γ (keV) ^a	I_γ (%) ^b	R^c	P	Multipolarity	Assignment	Band
122.9	1.4	0.33(4)		$M1/E2$	$9^- \rightarrow 8^-$	3 \rightarrow 4
186.4	<1				$11^- \rightarrow 10^-$	3 \rightarrow 4
214.2	3.6	0.56(4)		$M1/E2$	$6^+ \rightarrow 6^+$	6 \rightarrow 1
228.0	5.2	0.89(4)		$E2$	$9^- \rightarrow 7^-$	3
238.0	3.4				$18^+ \rightarrow 18^+$	8 \rightarrow 1a
242.9	2.0	0.47(2)		$M1/E2$	$13^- \rightarrow 12^-$	3 \rightarrow 4
252.8	2.3	0.60(2)		$M1/E2$	$8^+ \rightarrow 7^+$	10
262.0	1.8	0.81(15)		$M1/E2$	$19^- \rightarrow 18^-$	3 \rightarrow 4
265.7	1.7	1.19(5) ^d		$E1$	$8^- \rightarrow 8^+$	4 \rightarrow 10
278.0	<1				$14^- \rightarrow 14^+$	4 \rightarrow 6
293.4	9.8	0.84(2)	-0.02(10)	$M1/E2$	$6^+ \rightarrow 6^+$	10 \rightarrow 1
295.8	1.3	0.40(4)		$M1/E2$	$7^+ \rightarrow 6^+$	10 \rightarrow 9
307.2	1.4	0.56(4)		$M1/E2$	$15^- \rightarrow 14^-$	3 \rightarrow 4
308.9	1.2				$17^{(-)} \rightarrow 16^{(+)}$	5 \rightarrow 2
311.0	4.5				$16^+ \rightarrow 16^+$	8 \rightarrow 1a
318.8	1.3	0.74(4)		$M1/E2$	$17^- \rightarrow 16^-$	3 \rightarrow 4
324.6	1.0	0.84(4)		$E1$	$8^- \rightarrow 8^+$	4 \rightarrow 1
328.0	6.4	0.93(2) ^e		$E2$	$6^+ \rightarrow 4^+$	10 \rightarrow 9
332.8	<1				$12^- \rightarrow 12^+$	4 \rightarrow 6
388.8	23.4	0.64(2)	0.39(11)	$E1$	$9^- \rightarrow 8^+$	3 \rightarrow 10
430.9	2.9	0.75(3) ^f	0.20(19) ^g	$M1/E2$	$10^- \rightarrow 9^-$	4 \rightarrow 3
447.4	41.5	0.64(2)	0.02(9)	$E1$	$9^- \rightarrow 8^+$	3 \rightarrow 1
466.6	4.3	0.59(2)		$E1$	$22^+ \rightarrow 21^-$	2 \rightarrow 3
478.6	2.5	0.33(4)		$M1/E2$	$14^- \rightarrow 13^-$	4 \rightarrow 3
483.7	1.5	0.16(2)		$M1/E2$	$12^- \rightarrow 11^-$	4 \rightarrow 3
512.7	6.5	0.51(3) ^d		$M1/E2$	$4^+ \rightarrow 4^+$	6 \rightarrow 1
519.0	8.3	0.59(2)		$E1$	$8^- \rightarrow 7^+$	4 \rightarrow 10
524.7	11.8	0.88(3) ^f	0.21(17) ^g	$M1/E2$	$6^+ \rightarrow 4^+$	6
525.0	7.2	0.88(3) ^f	0.21(17) ^g	$E1$	$8^- \rightarrow 8^+$	4 \rightarrow 6
525.0	6.1	0.88(3) ^f	0.21(17) ^g	$E2$	$20^+ \rightarrow 18^+$	7 \rightarrow 8
533.0	<1				$12^+ \rightarrow 10^+$	1a
549.0	<1				$19^{(-)} \rightarrow 18^-$	5 \rightarrow 4
552.8	14.5	1.09(3)		$E2$	$10^- \rightarrow 8^-$	4
571.6	1.2				$11^- \rightarrow 10^+$	3 \rightarrow 6
573.3	10.0	0.39(2)		$M1/E2$	$7^+ \rightarrow 6^+$	10
576.1	<1				$13^- \rightarrow 12^+$	3 \rightarrow 6
584.9	<1				$15^- \rightarrow 14^+$	3 \rightarrow 6
592.8	10.3	0.58(2)		$E1$	$20^{(+)} \rightarrow 19^-$	2 \rightarrow 3
606.5	1.1	1.03(3) ^d		$E2$	$6^+ \rightarrow 4^+$	9
613.0	2.4	0.96(3) ^d		$E2$	$4^+ \rightarrow 2^+$	9
617.7	78.5	1.04(2)	0.55(9)	$E2$	$11^- \rightarrow 9^-$	3
646.5	11.3	0.89(3) ^f	0.22(17) ^g	$E1$	$9^- \rightarrow 8^+$	3 \rightarrow 6
648.8	15.6	0.89(3) ^f	0.22(17) ^g	$E2$	$8^+ \rightarrow 6^+$	6
657.2	$\equiv 100$	0.86(2)	0.01(12)	$E2$	$2^+ \rightarrow 0^+$	1
668.5	5.9	0.91(3) ^f		$M1/E2$	$17^{(-)} \rightarrow 16^-$	5 \rightarrow 4
670.9	9.5	0.91(3) ^f		$E2$	$12^- \rightarrow 10^-$	4
675.0	<1				$16^- \rightarrow 15^-$	4 \rightarrow 3
687.5	9.0	0.99(2)	0.61(33)	$E2$	$14^+ \rightarrow 12^+$	1a
693.2	2.5				$10^+ \rightarrow 8^+$	6
722.0	16.0	1.02(6)		$E2$	$14^- \rightarrow 12^-$	4
723.0	<1				$18^+ \rightarrow 17^-$	1a \rightarrow 3
723.0	<1				$12^+ \rightarrow 10^+$	6
725.0	<1				$18^- \rightarrow 17^-$	4 \rightarrow 3
725.1	11.1	1.09(2) ^f	0.65(11)	$E2$	$18^{(+)} \rightarrow 16^{(+)}$	2
727.8	68.0	1.09(2) ^f	0.65(11)	$E2$	$13^- \rightarrow 11^-$	3
744.2	<1				$20^+ \rightarrow 19^-$	1a \rightarrow 3

TABLE I. (*Continued.*)

E_γ (keV) ^a	I_γ (%) ^b	R^c	P	Multipolarity	Assignment	Band
744.3	91.3	0.86(2)	0.39(13)	$E2$	$4^+ \rightarrow 2^+$	1
762.2	4.3	1.29(6) ^f		$E2$	$20^+ \rightarrow 18^+$	7 \rightarrow 1a
762.8	14.0	1.29(6) ^f		$E2$	$16^+ \rightarrow 14^+$	1a
766.9	18.7	0.56(2)		$E1$	$18^{(+)} \rightarrow 17^-$	2 \rightarrow 3
772.5	4.4	0.63(4)		$E1$	$16^+ \rightarrow 15^-$	1a \rightarrow 3
777.1	<1				$14^+ \rightarrow 12^+$	6
785.8	63.0	1.00(2)		$E2$	$15^- \rightarrow 13^-$	3
789.5	4.4	0.53(7) ^d		$M1/E2$	$4^+ \rightarrow 4^+$	9 \rightarrow 1
794.3	5.1	0.65(3)		$E1$	$14^+ \rightarrow 13^-$	1a \rightarrow 3
812.5	16.2	1.03(2)	0.46(12)	$E2$	$20^{(+)} \rightarrow 18^{(+)}$	2
824.0	61.3	0.96(2)	0.34(8)	$E2$	$6^+ \rightarrow 4^+$	1
826.4	22.7				$8^+ \rightarrow 6^+$	10
835.5	4.2	0.59(2)		$E1$	$12^+ \rightarrow 11^-$	1a \rightarrow 3
862.1	3.0	0.73(6) ^e		$E2$	$8^+ \rightarrow 6^+$	6 \rightarrow 1
870.0	6.1				$18^+ \rightarrow 16^+$	8
875.0	1.2	1.07(6)		$E2$	$28^+ \rightarrow 26^+$	2a
884.0	4.1	1.26(8)		$E2$	$22^+ \rightarrow 20^+$	7
897.5	4.0				$26^+ \rightarrow 24^+$	2
921.0	<1				$2^+ \rightarrow 2^+$	9 \rightarrow 1
921.0	<1				$10^+ \rightarrow 9^-$	1a \rightarrow 3
924.0	3.9	1.12(4)		$E2$	$19^{(-)} \rightarrow 17^{(-)}$	5
943.3	12.5	1.26(2)		$E2$	$18^+ \rightarrow 16^+$	1a
970.6	21.3	1.05(2)	0.41(16)	$E2$	$22^{(+)} \rightarrow 20^{(+)}$	2
983.4	11.9	0.99(2)		$E2$	$16^- \rightarrow 14^-$	4
986.9	17.6	0.98(2)		$E2$	$19^- \rightarrow 17^-$	3
993.3	42.1	1.05(2)	0.55(11)	$E2$	$17^- \rightarrow 15^-$	3
999.0	<1				$28^{(+)} \rightarrow 26^{(+)}$	2
1007.7	11.0	0.97(3)		$E2$	$20^+ \rightarrow 18^+$	1a
1035.5	8.6	0.63(2)		$E1$	$16^{(+)} \rightarrow 15^-$	2 \rightarrow 3
1038.4	4.1				$6^+ \rightarrow 4^+$	6 \rightarrow 4
1043.9	8.1	1.14(6)		$E2$	$18^- \rightarrow 16^-$	4
1048.0	4.0				$28^{(+)} \rightarrow 26^{(+)}$	2a \rightarrow 2
1056.0	3.1				$(21^-) \rightarrow 19^{(-)}$	5
1061.8	48.0	0.95(2)	0.28(8)	$E2$	$8^+ \rightarrow 6^+$	1
1062.1	12.9	1.15(5)		$E2$	$24^{(+)} \rightarrow 22^{(+)}$	2
1071.5	9.3	1.22(5)		$E2$	$26^{(+)} \rightarrow 24^{(+)}$	2a \rightarrow 2
1074.2	3.2				$16^+ \rightarrow 14^+$	8 \rightarrow 1a
1094.4	11.5	1.00(4)		$E2$	$22^+ \rightarrow 20^+$	1a
1096.4	3.9	0.98(4)		$E2$	$21^- \rightarrow 19^-$	3
1103.0	<1				$(23^-) \rightarrow 21^-$	3
1106.0	7.6	1.04(5)		$E2$	$24^+ \rightarrow 22^+$	1a
1112.3	2.8				$(23^- \rightarrow 21^-)$	5
1118.0	15.4	0.99(3)		$E2$	$6^+ \rightarrow 4^+$	10 \rightarrow 1
1258.2	4.8	0.92(3)		$E2$	$4^+ \rightarrow 2^+$	6 \rightarrow 1
1281.1	4.5	0.50(2)		$E1$	$7^- \rightarrow 6^+$	3 \rightarrow 1
1293.1	1.1				$(26^+) \rightarrow 24^+$	1a
1368.0	<1				$10^+ \rightarrow 8^+$	1a \rightarrow 1

^aEnergies are estimated to be accurate to ± 0.3 keV.

^bThe relative transition intensities were extracted from γ - γ coincidence intensities from a two-dimensional projection of the hypercube. Errors on the relative intensities are typically $\leq 10\%$.

^cAngular-intensity ratios were obtained from the sum of gates on the 657 and 745 keV quadrupole transitions, unless otherwise indicated.

^dObtained by gating on the 553 keV quadrupole transition.

^eObtained by gating on the 618 keV quadrupole transition.

^fObtained from composite peak.

^gObtained from composite peak.

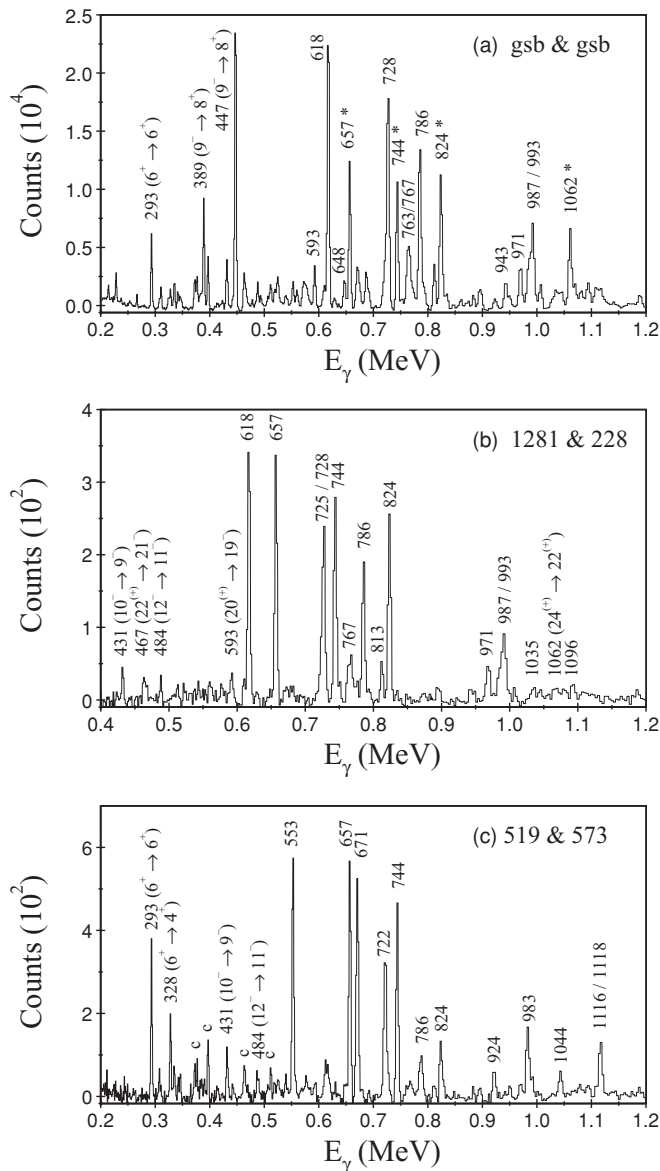


FIG. 6. Background-subtracted, double-gated, γ^3 spectra. The gates are (a) a list of ground-state band (gsb) transitions (labeled by asterisks) against itself; (b) the 1281 keV ($7^- \rightarrow 6^+$) transition against the 228 keV ($9^- \rightarrow 7^-$) transition, enhancing band 3; (c) the 519 keV ($8^- \rightarrow 7^+$) transition against the 573 keV ($7^+ \rightarrow 6^+$) transition, enhancing band 4. Contaminant peaks from ^{109}Sb ($\alpha 3p$) are labeled by ‘c’.

γ^4 analysis that the 533 and 1368 keV transitions could be placed with some confidence. Above spin 12^+ positive parity, band 1a carries a significant amount of intensity and is easily identifiable in coincidence spectra, see Fig. 6(a). It is observed to be fed by a number of structures, e.g., bands 7 and 8.

2. Bands 2 and 2a

Band 2 is built on a $16^{(+)}$ bandhead. The (tentative) positive-parity assignment has been inferred using the angular-intensity ratios which suggest an $E1$ character for the linking transitions to negative-parity band 3. Unfortunately, the insensitivity of

the linear-polarization measurement precluded a meaningful analysis, which would have provided a definitive answer. Band 2 is observed to be yrast above spin $18^{(+)}$. In the present work, the band has been extended to $28^{(+)}$, including the placement of a 1062 keV transition ($24^{(+)} \rightarrow 22^{(+)}$) that forms a self-coincident doublet with the strong 1062 keV transition ($8^+ \rightarrow 6^+$) of band 1. Intensity is seen to feed into this band above $24^{(+)}$, from band 2a. A spectrum showing transitions in band 2 is illustrated in Fig. 6(b).

3. Band 6

The structure labeled band 6, which strongly feeds yrast band 1 via a number of stretched and nonstretched $E2$ transitions has been significantly extended. Band 6 is built on a proposed 4^+ bandhead and extends up to a tentative spin of 16^+ , with the addition of four new in-band transitions. Proposed $E1$ decays link this structure to negative-parity bands 3 and 4. Intensity is observed to rapidly reduce in band 6 above 8^+ , making firm spin-parity/assignments difficult above 10^+ . A new 494 keV transition of proposed $E2$ character is observed to feed the 8^+ state in yrast band 1.

4. Bands 7 and 8

Band 7 is observed to be built on a proposed 20^+ bandhead. The $16^+ \rightarrow 14^+$ 763 keV transition in band 1a has been identified to be a self-coincident doublet with the 762 keV transition linking band 7 to band 1a. Band 7 is also observed to decay into another structure, labeled 8, through a 525 keV transition which forms a self-coincident triplet with transitions in, and feeding, band 6. Band 8 was established after the observation of a relatively intense 1074 keV transition feeding the 14^+ state of band 1a. Above the bandhead, a single 870 keV transition is observed. The structure decays back into band 1a via two transitions of energy 238 and 311 keV.

5. Bands 9 and 10

At low spin, sequences of positive-parity states observed to the left and right of band 1 have been confirmed and extended. Band 9 is assigned a 2^+ bandhead from the angular-correlation analysis and consists of two $E2$ transitions of similar energy (613 and 607 keV). The 607 and 296 keV transitions connecting band 9 to band 10 are newly identified, and taken with the stretched quadrupole nature of the 328 keV transition also linking bands 9 and 10, support the present spin-parity assignments of band 9. Note that these assignments differ from those of previous work [8]. Band 10 consists of even- and odd-spin positive-parity states, which are strongly fed by negative-parity band 3 and, to a lesser extent, band 4.

B. Low-spin negative-parity structures

1. Bands 3 and 4

Coincidence γ -ray spectra for bands 3 and 4 are shown in Figs. 6(b) and 6(c), respectively. Band 3 was postulated in Ref. [8] to be built on a 9^- bandhead. This assignment was confirmed after the electric dipole nature of the 389 and 447 keV transitions, which link band 3 to band 1, was

established from linear-polarization results. Band 3 is observed to be yrast at moderate spin. An additional 1103 keV transition, assumed to be $E2$ in character, has been added to the top of band 3, extending this structure to (23^-) . At spins 15^- and above, band 2 decays into this negative-parity yrast structure.

Band 3 is observed to be weakly linked to another negative-parity structure, labeled 4, by a number of $M1/E2$ transitions. Band 4 is built on a confirmed 8^- bandhead, which decays out through three different routes consisting of 325, 519, and 525 keV transitions, feeding bands 1, 10, and 6, respectively. The $E1$ nature of these transitions has, where possible, been confirmed. Band 4 is extended above 16^- with the addition of 1044 and 1116 keV $E2$ transitions up to a spin of 20^- .

Below the 9^- bandhead of band 3, a further 7^- state is observed. It decays to band 1 via a 1281 keV $E1$ transition. A relatively intense 228 keV $E2$ transition connects the 9^- and 7^- states. There is no evidence for a transition connecting the 8^- bandhead of band 4 to the 7^- state. This transition, however, would be very low in energy, which provides a possible explanation of why it has not been observed.

2. Band 5

Above the 16^- transition in band 4, intensity is observed to feed in from another structure of undetermined parity, labeled band 5. The 671 keV transition in band 4 is observed to be a self-coincident doublet with a 669 keV γ ray that is proposed to link band 4 to band 5. The choice of the 669 keV transition as the link to band 4 was confirmed by the observation of a weak 549 keV transition linking the $19^{(-)}$ state in band 5 to the 18^- state in band 4. The 924 keV transition, previously assigned to band 4 [8], is now assigned to band 5. Band 5 continues up to a probable spin of $23^{(-)}$.

V. DISCUSSION

A. Experimental alignments and Routhians

The experimental alignments i_x for the bands of ^{110}Te are shown in Fig. 7. To obtain these quantities, it is necessary to

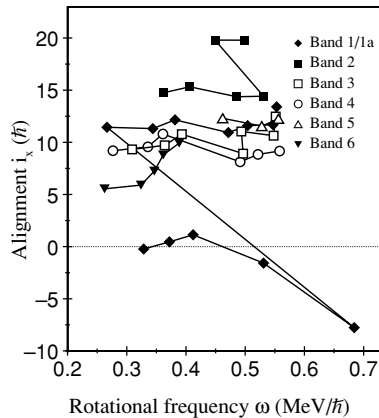


FIG. 7. Alignment plot for the low-spin bands in ^{110}Te . Positive-parity states are labeled with filled symbols, negative-parity states with open symbols.

transform the experimental data into the intrinsic frame of the nucleus. This requires the subtraction of a core contribution, leaving the single-particle energy and spin contributions solely from the valence nucleons. The experimental alignment can be written [18]

$$i_x(\omega) = I_x(\omega) - I_{x,\text{ref}}(\omega). \quad (3)$$

The reference $I_{x,\text{ref}}(\omega)$ is generally obtained from the ground-state band of a rotational even-even nucleus. The assumption at low spin that the nuclear moment of inertia is proportional to the square of the rotational frequency is used to define an energy reference based on a variable moment of inertia [19],

$$\mathcal{J}_{\text{ref}}^{(1)} = \mathcal{J}_0 + \mathcal{J}_1 \omega^2. \quad (4)$$

\mathcal{J}_0 and \mathcal{J}_1 are Harris parameters which are obtained by a fit to the reference band.

The nucleus ^{110}Te has a vibrational ground-state band structure which prevents the extraction of good Harris parameters; therefore, a reasonable fit has been made to transitions in band 3. The rotational reference $I_{x,\text{ref}}$ is hence defined by

$$I_{x,\text{ref}}(\omega) = \omega(\mathcal{J}_0 + \mathcal{J}_1 \omega^2) - i_0. \quad (5)$$

Harris parameters $\mathcal{J}_0 = 18.6$ and $\mathcal{J}_1 = 31.3\hbar^4 \text{ MeV}^{-3}$ have subsequently been extracted together with $i_0 = 5\hbar$. These values provide a reasonable reference over the whole frequency range. The resulting alignment plot for bands 1–6 in ^{110}Te is shown in Fig. 7.

The experimental Routhian can be expressed as [18]

$$e'(I) = E_{\text{expt}}^\omega(I) - E_{\text{ref}}^\omega(I) \quad (6)$$

and represents the energy in the rotating frame. A plot showing the Routhian e' as a function of rotational frequency ω for band 1/1a is illustrated in Fig. 8 and shows a band crossing (labeled ω_{ef}) between the zero-quasiparticle ground-state band (band 1) and a two-quasiparticle configuration (band 6).

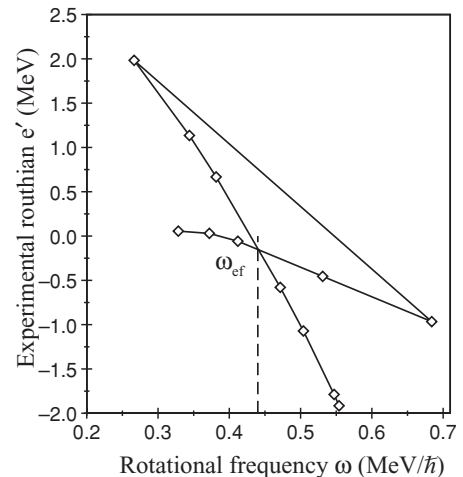


FIG. 8. Experimental Routhians for bands 1 and 1a.

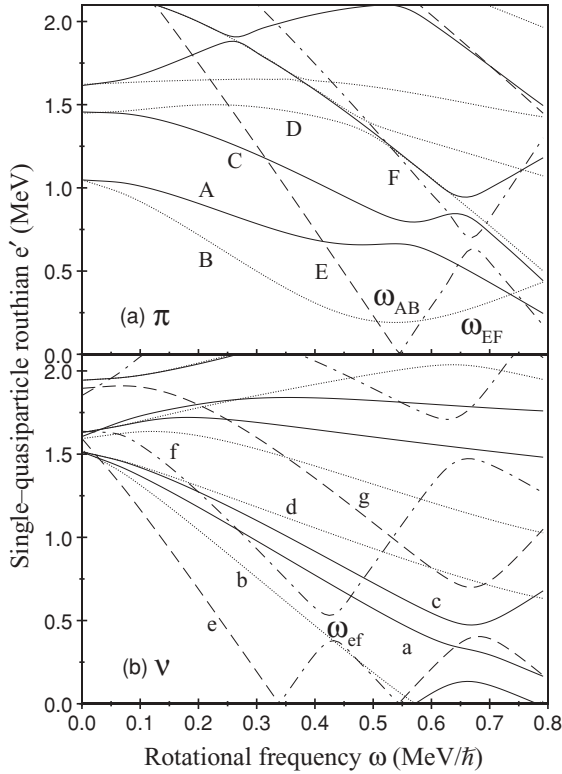


FIG. 9. Theoretical single-quasiparticle levels for ^{110}Te . Solid lines show levels with $(\pi, \alpha) = (+, +1/2)$; dotted lines, $(+, -1/2)$ levels; dashed lines, $(-, -1/2)$ levels; and dot-dashed lines, $(-, +1/2)$ levels. The calculations used the modified Nilsson potential with deformation parameters $\varepsilon_2 = 0.135$, $\varepsilon_4 = -0.04$, and $\gamma = 0^\circ$. The pairing gaps used were $\Delta_p = 1.030$ MeV and $\Delta_n = 1.420$ MeV. Band-crossing frequencies (ω_{AB} , ω_{EF} , ω_{ef}) are denoted.

B. Cranked shell-model calculations

Cranked shell-model calculations, using a modified oscillator potential with the Nilsson parameters of Ref. [20], have been performed for ^{110}Te in order to provide further theoretical interpretation of the low- to medium-spin regime. Representative results are shown in Fig. 9, and the orbital labeling adopted here is listed in Table II. The calculations were

TABLE II. Labeling of single-quasiparticle orbitals adopted in this paper.

(Parity, signature)	Protons		Neutrons	
	Label	Dominant shell-model state	Label	Dominant shell-model state
$(+, +1/2)_1$	A	$g_{7/2}$	a	$g_{7/2}$
$(+, -1/2)_1$	B	$g_{7/2}$	b	$g_{7/2}$
$(+, +1/2)_2$	C	$d_{5/2}$	c	$d_{5/2}$
$(+, -1/2)_2$	D	$d_{5/2}$	d	$d_{5/2}$
$(-, -1/2)_1$	E	$h_{11/2}$	e	$h_{11/2}$
$(-, +1/2)_1$	F	$h_{11/2}$	f	$h_{11/2}$
$(-, -1/2)_2$	G	$h_{11/2}$	g	$h_{11/2}$

performed for both protons and neutrons using a set of input parameters derived from deformation self-consistent cranking calculations, based on the total Routhian surface (TRS) formalism [21–23]. The TRS results show that configurations in ^{110}Te have a quadrupole deformation of $\varepsilon_2 \approx 0.130$, $\gamma \approx 0^\circ$ at low spin which gradually increases as a function of rotational frequency to $\varepsilon_2 \approx 0.140$, $\gamma \approx 7^\circ$ at $\omega = 0.50$ MeV/ \hbar . For the purpose of the cranked shell-model calculations, deformation parameters $\varepsilon_2 = 0.135$, $\varepsilon_4 = -0.04$, and $\gamma = 0^\circ$ were used.

C. Band assignments

1. Positive-parity bands: Bands 1 and 1a

The proximity of the neutron-deficient tellurium isotopes to the $Z = N = 50$ doubly closed shell means that the limited number of valence particles outside of the closed core is unable to induce significant static deformation and rotational collectivity. Tellurium isotopes are therefore expected to possess only moderate quadrupole ground-state deformation and hence a low-spin decay scheme dominated by single-particle and vibrational effects. In common with other even tellurium isotopes, band 1, the ground-state band in ^{110}Te appears more vibrational rather than rotational in character. Indeed, the $E(4^+)/E(2^+)$ energy ratio (2.13) in ^{110}Te is much closer to the pure vibrational limit (2.00) than the rotational limit (3.33). Moreover, the low-lying states with $I^\pi \leq 8^+$ in the even tellurium isotopes have been interpreted in terms of phonon states where $\pi[g_{7/2}]^2$ or $\pi[g_{7/2} \otimes d_{5/2}]$ proton configurations are coupled to the spherical ($Z = 50$) tin core states [24,25].

Above spin 8^+ , a sharp drop in intensity is observed in bands 1/1a coinciding with the structure becoming nonyrast. Inspection of the alignment plot of Fig. 7 reveals a sharp backbend, indicating that a particle alignment has taken place. In common with other even tellurium isotopes, the positive-parity states above 10^+ can be interpreted in terms of an aligned $\nu[h_{11/2}]^2$ configuration. Figure 7 reveals that band 1 gains $10\hbar$ in alignment before continuing as positive-parity band 1a. The experimental crossing frequency for the alignment is shown in the Routhian plot of Fig. 8 and occurs at a frequency $\omega = 0.44$ MeV/ \hbar . Comparison with the cranked shell-model calculations shows that a pair of $h_{11/2}$ quasineutrons are predicted to align at this frequency, i.e., $\omega_{ef} = 0.44$ MeV/ \hbar .

In other even tellurium isotopes the positive-parity $\nu[h_{11/2}]^2$ configuration is observed yrast up to high spin; however, this is not the case in ^{110}Te . In this neutron-deficient nucleus, the neutron Fermi surface ($N = 58$) lies below the $\nu h_{11/2}$ subshell. This makes the $\nu[h_{11/2}]^2$ configuration less energetically favorable, thus allowing negative-parity structures (bands 3 and 4) to compete and become yrast around $I = 10$.

2. Positive-parity bands: Band 6

Band 6 is a positive-parity structure with a 4^+ bandhead extending in spin above the $\nu[h_{11/2}]^2$ alignment with decreasing intensity up to a tentative (16^+). The alignment plot illustrated in Fig. 7 implies band 6 is rotational in nature with the γ -ray

energies increasing smoothly with spin. In this regard, band 6 behaves similarly to the high-spin terminating bands seen throughout this mass region, which are based on deformed particle-hole excitations across the $Z = 50$ shell gap. Indeed, such high-spin structures in ^{110}Te are presented in Ref. [10].

3. Negative-parity bands: Bands 3 and 4

Negative-parity bands 3 and 4 are populated with significant intensity in ^{110}Te , in marked contrast to other (heavier) even tellurium isotopes. ^{110}Te thus provides a unique opportunity to investigate these negative-parity structures since their population intensity has allowed a detailed spectroscopic study of the bands, which included the observation of a number of interlinking magnetic dipole transitions.

The experimental alignment plot, Fig. 7, shows that bands 3 and 4 have similar alignments, which is typical of signature partner bands. Both structures show an initial alignment less than that of the $\nu[h_{11/2}]^2$ configuration. This implies a two-quasineutron configuration involving one $h_{11/2}$ neutron coupled to a positive-parity orbital.

Below the 9^- bandhead of band 3, a low-lying 7^- state is observed which decays back to the yrast low-spin structure via a 1281 keV $E1$ transition. Such low-lying states have been observed in a number of even tellurium nuclei (^{112}Te – ^{132}Te) [25] and they have been explained in terms of a low-lying two-quasiparticle state. This involves the $h_{11/2}$ orbital in a two-quasineutron $\nu[h_{11/2} \otimes d_{5/2}]_{7^-}$ configuration.

In this mass region, the $[411]3/2^+$ and $[413]5/2^+$ Nilsson orbitals, derived predominantly from $\nu d_{5/2}$ and $\nu g_{7/2}$ states, respectively, are almost degenerate. The cranked shell-model quasineutron of Fig. 9(b) shows how close these orbitals (a, b, c, d) are at low frequency. The most energetically favored positive-parity orbital is the b orbital ($g_{7/2}$), with signature $\alpha = -1/2$. Coupling this orbital to the $\alpha = -1/2$ e orbital ($h_{11/2}$) yields the yrast negative-parity band (be) with signature $\alpha = 1$, or odd spins, i.e., band 3. Band 4 is then formed by the $\alpha = 0$ ae configuration.

D. Analysis of γ -ray branching ratios

$B(M1; I \rightarrow I - 1)/B(E2; I \rightarrow I - 2)$ and $B(E1; I \rightarrow I - 1)/B(E2; I \rightarrow I - 2)$ ratios of reduced transition probabilities may be readily extracted from experimental γ -ray branching ratios of competing $\Delta I = 1$ and $\Delta I = 2$ transitions. From the present data, γ -ray spectra were produced by placing a double coincidence requirement on the two transitions lying above each state of interest, in order to ensure good quality spectra were obtained. The branching ratio, $\lambda = I_\gamma(\Delta I = 2)/I_\gamma(\Delta I = 1)$, of the competing quadrupole and dipole transitions depopulating that level was then measured.

The ratios of reduced transition probabilities were determined as

$$\frac{B(M1)}{B(E2)} \equiv \frac{B(M1; I \rightarrow I - 1)}{B(E2; I \rightarrow I - 2)} = \frac{1}{1.43 \times 10^4} \frac{1}{\lambda} \times \frac{[E_\gamma(\Delta I = 2)]^5}{[E_\gamma(\Delta I = 1)]^3} (\mu_N^2 e^{-2} \text{fm}^{-4}), \quad (7)$$

and

$$\frac{B(E1)}{B(E2)} \equiv \frac{B(E1; I \rightarrow I - 1)}{B(E2; I \rightarrow I - 2)} = \frac{1}{1.3 \times 10^6} \frac{1}{\lambda} \times \frac{[E_\gamma(\Delta I = 2)]^5}{[E_\gamma(\Delta I = 1)]^3} (\text{fm}^{-2}), \quad (8)$$

respectively, with γ -ray energies in MeV. The $\Delta I = 1$ transitions were assumed to be pure stretched dipole in character with no quadrupole admixture ($\delta \equiv 0$). For nonzero δ , Eqs. (7) and (8) should be modified by a factor $(1 + \delta^2)^{-1}$ but are insensitive to δ since typically $\delta^2 \ll 1$. Moreover, the errors introduced by the experimental branching ratios λ are usually significantly larger than the effect of neglecting δ , particularly in the present case where the relevant transitions are weak.

$B(M1)$ and $B(E1)$ values have also been extracted by using the following expression as an estimate for the $B(E2)$ rate,

$$B(E2; I \rightarrow I - 2) = \frac{5}{16\pi} Q_0^2 |(IK20|I - 2K)|^2, \quad (9)$$

obtained from the rotational model [26]. Although ^{110}Te is not a good rotor, we have used an average quadrupole moment, $Q_0 = 200 e \text{fm}^2$, to determine the $B(E2)$ values. This value of quadrupole moment was determined from the predicted average quadrupole deformation of $\varepsilon_2 = 0.135$ for ^{110}Te , see Sec. V B.

1. $B(M1)/B(E2)$ ratios

$B(M1)/B(E2)$ ratios are extremely useful in assigning single-particle configurations. Such ratios have been extracted for the negative-parity bands 3/4 and are listed in Table III. $B(M1)$ strengths have also been extracted, as listed in Table III, together with estimates of $|g_K - g_R|$ obtained from the equation

$$B(M1; I \rightarrow I - 1) = \frac{3}{4\pi} (g_K - g_R)^2 \mu_N^2 K^2 \times |(IK10|I - 1K)|^2, \quad (10)$$

which is valid for $K \neq 1/2$.

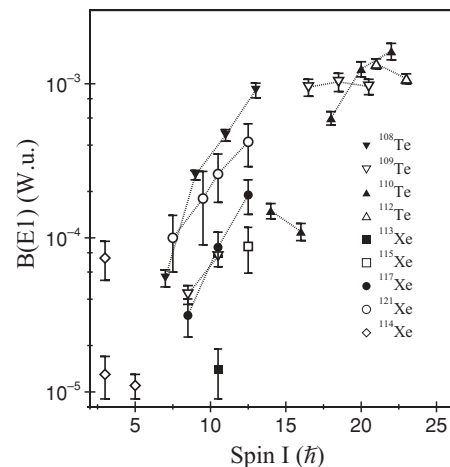


FIG. 10. $B(E1)$ results deduced for ^{110}Te and neighboring nuclei.

TABLE III. Measured $B(M1)/B(E2)$ ratios and magnetic dipole strengths, deduced from the rotational model, in ^{110}Te coupled bands 3 and 4.

E_γ (keV)	I^π Initial	Band	$B(M1)/B(E2)$ ($10^{-3} \mu_N^2 e^{-2} \text{fm}^{-4}$)	$B(M1)$ (μ_N^2)	$B(M1)$ (W.u.)	$ g_K - g_R $
123	9^-	$3 \rightarrow 4$				
431 ^a	10^-	$4 \rightarrow 3$	0.005(1)	0.006(1)	0.003(5)	0.12(1)
186	11^-	$3 \rightarrow 4$	0.017(5)	0.021(6)	0.012(4)	0.22(4)
484	12^-	$4 \rightarrow 3$	0.012(3)	0.015(3)	0.009(2)	0.19(2)
243	13^-	$3 \rightarrow 4$	0.019(8)	0.025(8)	0.014(4)	0.24(3)
479	14^-	$4 \rightarrow 3$	0.020(4)	0.027(5)	0.015(3)	0.24(3)
307	15^-	$3 \rightarrow 4$	0.011(4)	0.015(4)	0.008(3)	0.18(3)
319	17^-	$3 \rightarrow 4$	0.015(2)	0.020(3)	0.011(1)	0.21(1)

^aSelf-coincident doublet.

2. $B(E1)/B(E2)$ ratios

$B(E1)/B(E2)$ ratios have been extracted for the $E1$ transitions linking bands 1a and 3, and bands 2 and 3. $B(E1)$ strengths have also been deduced. The results are listed in Table IV. In the scenario of octupole collectivity, an estimate of the size of the intrinsic dipole moment D_0 can be obtained, using the approach of Ref. [27], with the equation

$$B(E1; I \rightarrow I - 1) = \frac{3}{4\pi} D_0^2 |(IK10|I - 1K)|^2. \quad (11)$$

Values of $|D_0|$ extracted for ^{110}Te are included in Table IV.

E. $B(E1)$ strengths and octupole effects

The extracted $B(E1)$ strengths in ^{110}Te are listed in Table IV and are compared in Fig. 10 with those for the neighboring ^{108}Te [28], ^{109}Te [29], ^{112}Te [30], ^{113}Xe [31], ^{114}Xe [32], ^{115}Xe [33], ^{117}Xe [34], and ^{121}Xe [35] isotopes.

Inspection of Fig. 10 reveals that the strongest $B(E1)$ strengths are observed in the near-spherical tellurium isotopes with $B(E1) \sim 10^{-3}$ W.u. for spin $\sim 20\hbar$. Indeed, the $B(E1)$ strengths obtained for ^{110}Te are the largest of all the tellurium isotopes. This value is similar to those found in the neutron-rich barium isotopes which lie on an octupole magic number ($Z = 56$). The values obtained are slightly smaller than those observed in the Ra-Th region [36,37], the most well-developed region for octupole effects. In comparison, the $B(E1)$ strengths for the light xenon isotopes are considerably weaker.

Octupole correlations lead to enhanced $E1$ strength in nuclei. Indeed, the observation of such $E1$ strength [usually taken as $B(E1) > 10^{-5}$ W.u] is often cited as evidence for octupole correlations in nuclei. The octupole correlations may be either static (deformation) or dynamic (vibrational) in nature. In this mass region, octupole collectivity may be expected since both proton and neutron orbitals with $\Delta N_{\text{osc}} = 1$ and $\Delta j = \Delta l = 3$ ($h_{11/2}$ and $d_{5/2}$) are near the Fermi surface. The strongest effects have been calculated for barium ($Z = 56$), xenon ($Z = 54$), and tellurium ($Z = 52$) isotopes with $N \approx 56$ [38]. These nuclei are predicted to show a softness with respect to octupole deformation in their ground states. Calculations using Hartree-Fock + BCS (static correlations) and generator-coordinate (dynamical correlations) methods [39] suggest that octupole collectivity is enhanced by dynamical correlations. It is also possible that rotation could enhance octupole effects, and it has been suggested that nuclei with dynamical octupole deformations at low spin could develop static octupole deformation at high spin [40].

VI. CONCLUSIONS

The Gammasphere γ -ray spectrometer, when used in conjunction with the Microball charged particle detector and a number of neutron detectors, has been shown to be an extremely powerful tool for the purpose of high-spin γ -ray spectroscopy studies.

TABLE IV. Measured $B(E1)/B(E2)$ ratios and electric dipole strengths, deduced from the rotational model, in ^{110}Te .

E_γ (keV)	I^π Initial	Band	$B(E1)/B(E2)$ (10^{-6}fm^{-2})	$B(E1)$ ($10^{-3} e^2 \text{fm}^2$)	$B(E1)$ 10^{-3} (W.u.)	$ D_0 $ (e fm)
767	$18^{(+)}$	$2 \rightarrow 3$	0.63 ^a	0.89 ^a	0.60 ^a	0.087 ^a
593	$20^{(+)}$	$2 \rightarrow 3$	1.31(11)	1.86(15)	1.25(10)	0.126(10)
467	$22^{(+)}$	$2 \rightarrow 3$	1.69(53)	2.41(74)	1.63(52)	0.144(46)
794	14^+	$1a \rightarrow 3$	0.15(2)	0.21(3)	0.15(2)	0.060(9)
773	16^+	$1a \rightarrow 3$	0.12(1)	0.16(1)	0.11(1)	0.037(3)

^aMeasurement from Ref. [8], uncertainty $< 10\%$.

High-spin states in the neutron-deficient ^{110}Te nucleus have been populated using the $\alpha 2p$ exit channel. The level scheme of this nucleus has been significantly extended. The large number of statistics obtained has allowed extremely weak structural features to be discerned, allowing a significant insight into how nuclei in close proximity to the $Z = 50$ shell gap behave with increasing values of angular momentum.

At low spin, the ^{110}Te level scheme appears vibrational similar to other tellurium isotopes. With increasing spin, the onset of octupole correlation effects, induced by the close proximity of both neutron and proton $h_{11/2}$ - $d_{5/2}$ orbitals to

the Fermi surface, has been postulated. Finally, new collective high-spin structures in ^{110}Te , found from the present work, are presented in the accompanying paper [10].

ACKNOWLEDGMENTS

This work was supported in part by the the U.K. Engineering and Physical Sciences Research Council, DOE Grant DE-F05-96ER-40983, the U.S. National Science Foundation, and the U.S. National Research Council under the Collaboration in Basic Science and Engineering Program.

-
- [1] R. Wadsworth *et al.*, Phys. Rev. C **53**, 2763 (1996).
 [2] H. Schnare *et al.*, Phys. Rev. C **54**, 1598 (1996).
 [3] B. Hadinia *et al.*, Phys. Rev. C **72**, 041303(R) (2005).
 [4] I. Ragnarsson, V. P. Janzen, D. B. Fossan, N. C. Schmeing, and R. Wadsworth, Phys. Rev. Lett. **74**, 3935 (1995).
 [5] A. V. Afanasjev, D. B. Fossan, G. J. Lane, and I. Ragnarsson, Phys. Rep. **322**, 1 (1999).
 [6] R. Wadsworth *et al.*, Phys. Rev. Lett. **80**, 1174 (1998).
 [7] E. S. Paul *et al.*, Phys. Rev. C **75**, 014308 (2007).
 [8] E. S. Paul *et al.*, Phys. Rev. C **50**, R534 (1994).
 [9] C. Fahlander *et al.*, Nucl. Phys. **A577**, 773 (1994).
 [10] E. S. Paul *et al.*, Phys. Rev. C **76**, 034323 (2007).
 [11] I. Y. Lee *et al.*, Nucl. Phys. **A520**, 641c (1990).
 [12] D. G. Sarantites *et al.*, Nucl. Instrum. Methods A **381**, 418 (1996).
 [13] D. Seweryniak *et al.*, Nucl. Instrum. Methods A **340**, 353 (1994).
 [14] D. C. Radford, Nucl. Instrum. Methods A **361**, 297 (1995); **361**, 306 (1995).
 [15] D. C. Radford, M. Cromaz, and C. J. Beyer, in *Proceedings of the Nuclear Structure '98 Conference, Gatlinburg, 1998*, AIP Conf. Proc. No. 481, edited by C. Baktash (AIP, New York, 1999), p. 570.
 [16] K. S. Krane, R. M. Steffen, and R. M. Wheeler, Nucl. Data Tables **11**, 351 (1973).
 [17] G. J. Schmid *et al.*, Nucl. Instrum. Methods A **417**, 95 (1998).
 [18] R. Bengtsson and S. Frauendorf, Nucl. Phys. **A327**, 139 (1979).
 [19] S. M. Harris, Phys. Rev. **138**, B509 (1965).
 [20] J. Y. Zhang, N. Xu, D. B. Fossan, Y. Liang, R. Ma, and E. S. Paul, Phys. Rev. C **39**, 714 (1989).
 [21] W. Nazarewicz, G. A. Leander, and J. Dudek, Nucl. Phys. **A467**, 437 (1987).
 [22] R. Wyss, J. Nyberg, A. Johnson, R. Bengtsson, and W. Nazarewicz, Phys. Lett. **B215**, 211 (1988).
 [23] W. Nazarewicz, R. Wyss, and A. Johnson, Nucl. Phys. **A503**, 285 (1989).
 [24] P. Chowdhury, W. F. Piel Jr., and D. B. Fossan, Phys. Rev. C **25**, 813 (1982).
 [25] T. Lonnroth, A. Vitanen, and J. Hattula, Phys. Scr. **34**, 682 (1986).
 [26] A. Bohr and B. R. Mottelson, *Nuclear Structure* (W. A. Benjamin, Inc., New York, 1975), Vol. II.
 [27] G. A. Leander, W. Nazarewicz, G. F. Bertsch, and J. Dudek, Nucl. Phys. **453**, 58 (1986).
 [28] G. J. Lane *et al.*, Phys. Rev. C **57**, R1022 (1998).
 [29] A. J. Boston *et al.*, Phys. Rev. C **61**, 064305 (2000).
 [30] E. S. Paul *et al.*, Phys. Rev. C **50**, 698 (1994).
 [31] H. C. Scraggs *et al.*, Phys. Rev. C **61**, 064316 (2000).
 [32] G. de Angelis *et al.*, Phys. Lett. **B535**, 93 (2002).
 [33] E. S. Paul, H. R. Andrews, T. E. Drake, J. DeGraaf, V. P. Janzen, S. Pilotte, D. C. Radford, and D. Ward, Phys. Rev. C **53**, 2520 (1996).
 [34] E. S. Paul *et al.*, Nucl. Phys. **A644**, 3 (1998).
 [35] J. Timár, J. Simpson, E. S. Paul, S. Araddad, C. W. Beausang, M. A. Bentley, M. J. Joyce, and J. F. Sharpey-Schafer, J. Phys. G **21**, 783 (1995).
 [36] P. A. Butler and W. Nazarewicz, Nucl. Phys. **A533**, 249 (1991).
 [37] P. A. Butler and W. Nazarewicz, Rev. Mod. Phys. **68**, 349 (1996).
 [38] J. Skalski, Phys. Lett. **B238**, 6 (1990).
 [39] P. -H. Heenen, J. Skalski, P. Bonche, and H. Flocard, Phys. Rev. C **50**, 802 (1994).
 [40] R. V. Jolos and P. von Brentano, Phys. Rev. C **49**, R2301 (1994).